

Transport simulations of the pre-thermal-quench phase in ASDEX Upgrade massive gas injection experiments

E. Fable, G. Pautasso, M. Lehnen¹, R. Dux, M. Bernert, A. Mlynek, and the ASDEX Upgrade Team

Max-Planck-Institut für Plasmaphysik, 85748 Garching, Germany

¹ ITER Organization, Route de Vinon sur Verdon, 13115 Saint Paul lez Durance, France

E-mail: emiliano.fable@ipp.mpg.de

Abstract. The pre-thermal-quench (PTQ) phase of the massive gas injection (MGI) scenario to terminate the tokamak plasma discharge is studied by means of 1D transport simulations. This phase is characterized by the cold-front penetration in the hot plasma after the gas has been released from the valves, and before the actual thermal quench takes place, with consequent plasma disruption at lower stored energy. The comparison between the simulations and the ASDEX Upgrade (AUG) experiments allows to gain insight in the observed dependencies and time scales. Despite the genuine 3D structure of the problem, it is shown that the 1D simulations are already giving experimentally relevant answers, the reason for which will be discussed in detail. Influence of unknown parameters and simplifying assumptions are also discussed.

1. Introduction

The massive injection of impurity gas, into a pre-disruptive plasma, is used in existing devices to induce a fast but mitigated termination of the discharge ([1] and [2]). The same technique is also foreseen for ITER and a Disruption Mitigation System (DMS) is being developed for this international tokamak (see ref.s [3] and [4] for details). The ITER DMS foresees both shattered pellet injection and MGI as mitigation techniques [4]. It is likely that many aspects of simulations of MGI rapid shutdown will also be relevant for SPI shutdown. Nevertheless the comparison between the two mitigation techniques can only be conducted on tokamak devices (DIII-D at the moment), on which both systems are available.

The injected impurities mitigate the impending disruption in three different ways. Firstly, they radiate part of the plasma thermal energy before this is conducted to and along the scrape-off-layer onto the divertor plates or limiting surfaces by the large thermal conductivity, typical of a natural thermal quench (TQ). Secondly, the current quench duration, the vertical force on the vessel and the eddy currents, in the machine components, can be tailored by varying the amount and type of impurities. Thirdly, the formation and dissipation of eventual runaway electrons can be influenced by the choice of the injected impurity amount and type.

The work described in the present paper is focused on the modelling of the initial phase of the interaction of the impurities with the plasma. In particular, the so called pre-thermal quench (pre-TQ) phase, that is the time between the arrival of the gas at the plasma edge and the onset of the induced TQ, is studied experimentally and theoretically.

The pre-TQ duration is a design parameter of the ITER DMS and must be known with good accuracy. In fact, it is the impurity gas (in the gaseous or frozen form) which is assimilated by the plasma in this time interval, that radiates the thermal energy, before the TQ sets in and during the TQ. An amount of impurities sufficient to mitigate most (90 % is quoted in [4]) of the thermal energy must be delivered to the plasma during this time; smaller amounts of gas could induce the rapid growth of MHD modes and the TQ onset without providing sufficient radiated power. The injector location (distance from the plasma) and orifice diameter, the gas pressure, along with the pre-TQ time, determine the thermal load mitigation efficiency.

Dedicated Massive Gas Injection (MGI) experiments were conducted in ASDEX Upgrade (AUG) in order to document the evolution of the pre-TQ for different target plasma (energy and safety factor) and gas (quantity and type; valve position) parameters. The same phase was then modelled with the transport code ASTRA, coupled with the radiation code STRAHL. The purpose of this article is to discuss and compare the simulation results with the experimental observations.

This work is the first benchmark of ASTRA against detailed MGI experimental measurements. The ultimate scope of the work is to verify if ASTRA provides a proper model for the pre-TQ prediction and, in the affirmative case, to use the code for

modelling the pre-TQ in ITER plasmas. Notice that MGI ITER plasmas simulations are also being carried out by S. Konovalov and team with the Russian code package ASTRA-ZIMPUR [5].

A code which models all aspects of MGI experiments and which allows extrapolation to ITER does not exist. The interaction between impurities and plasma is a complex 3D process in which energy and particle (ionized and neutral) transport, atomic physics, non-linear MHD and kinetic effects are involved. It is common opinion that 3-D non-linear MHD codes, like NIMROD ([6]) and JOREK ([7]) should be developed further for the purpose of modelling MGI. Although both codes have part of the MGI relevant physics built in already, these codes cannot be presently used for parameter scans and exploratory studies, consisting of numerous scenario modelling, since they consume a large amount of CPU time. Previous modelling of MGI with different 2-D transport codes (e.g. SOLPS-EIRENE [8], TOKES [9], and TokSys [10]) have been shown to reproduce the time scale of the pre-TQ and therefore encourage an extended benchmark of ASTRA-STRAHL against detailed AUG measurements.

The criterion determining the end of the pre-TQ is the onset of the TQ, i.e. a complex and "explosive" process. The hypothesis, that a threshold value of the current gradient at the $q=2$ surface is a proper proxy for the complex criterion determining the end of the pre-TQ, will have to be verified during the benchmark process. The sensitivity of the transport calculations to different diffusion coefficients must be tested; the experimental finding, that the pre-TQ phase duration does not depend on the target plasma thermal energy at relatively large amounts of injected particles, must be reproduced by the physics model.

The paper is structured in the following way: Section 2 is dedicated to the description of the fast MGI valves, of a selection of experimental results, which the ASTRA-STRAHL code package must model and explained, and of a few relevant diagnostics. The modeling set-up used inside the code package ASTRA-STRAHL is presented in Section 3. The numerical results and discussion of the physics processes involved are presented in Section 4. Conclusions will be drawn in Section 5.

2. Experiment setup

2.1. MGI valves

During the 2014 experimental campaign, the tokamak ASDEX Upgrade (AUG) was equipped with two fast valves located close to the plasma, one on the low field side of sector 13 (LFS-S13) and the second on the high field side of sector 4 (HFS-S4), toroidally displaced of an angle circa $\Delta\Phi = \pi$ from each other (AUG consists of 16 toroidal sectors).

The HFS valve is mounted 40 cm above the mid-plane and 10 cm behind the limiting surface defined by the heat shield (fig. 1). It has a gas reservoir volume of 85 cm³, an opening time of < 1 ms, a nozzle diameter of 13 mm and a maximum reservoir

pressure of 50 bar similar to the corresponding parameters of the older LFS valve [11], i.e. 80 cm^3 , 1 ms, 14 mm and 50 bar respectively. Both valves were designed to release most of the gas contained in the reservoir before the beginning of the current quench. The time delay between the trigger and the arrival of the gas at the plasma edge, as detected by the AXUV (Absolute eXtreme UltraViolet) diagnostic, is of the order of 1 ms. Assuming ideal flow, a movement of the stem linear in time and lasting 1.5 ms (which has been measured), the pressure in the valve and the quantity of gas released in the vessel have been calculated and are shown in fig. 2.

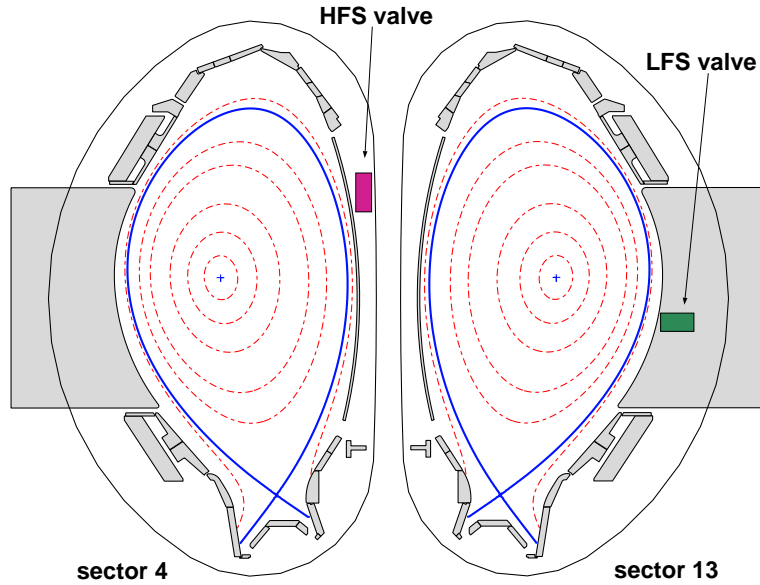


Figure 1. Location of the mitigation valves in the AUG vessel (year 2014).

2.2. Plasma scenarios

A dedicated experiment, consisting of 11 discharges, was carried out on AUG to document the evolution of the pre-TQ for different plasma and gas parameters. A description of the parameter scan follows; table 1 summarizes relevant gas, machine and target plasma parameters, along with some experimental results.

- Thermal energy scan.** Three plasmas with varying thermal energy, i.e. $E_{th} \sim 0.1$, 0.5 and 0.7 MJ, were generated with different combinations of ohmic heating (alone in the first case), NBI and ECRH input power. The equilibrium configurations of these discharges were comparable (lower single null plasma with low triangularity); the plasma current of 1 MA, the toroidal magnetic field of 2.5 T and the resultant $q_{95} \sim 4.3$ were held constant. The neon gas was injected with the two fast valves, LFS-S13 and HFS-S4, in order to distribute it toroidally.

- Gas quantity and valve position scan.** A maximum gas quantity of $8 \text{ kPa} \times \text{m}^3$ [4] is planned to be injected by the ITER DMS for the thermal quench mitigation. This quantity, divided by the ITER plasma volume of 830 m^3 corresponds to 80 % of (i.e. it

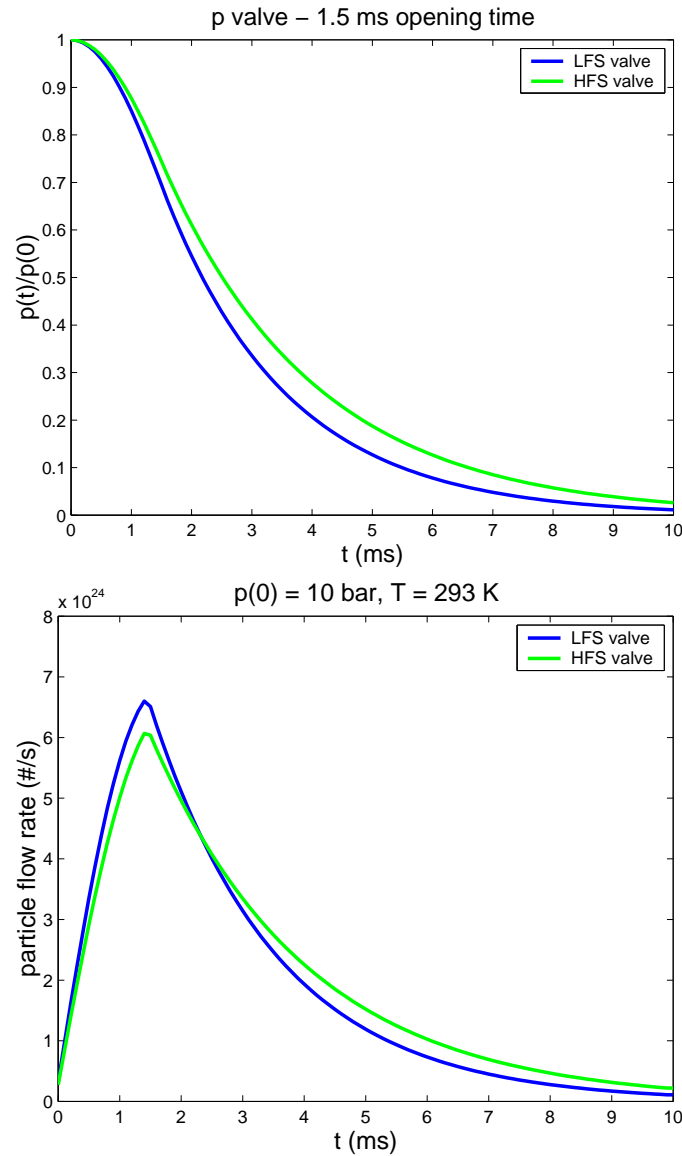


Figure 2. Time evolution of the pressure $p(t)/p(0)$ in the valve reservoir (above). Gas flow of neon from the AUG valves for an initial reservoir pressure of 10 bar or gas quantity of $0.85 \text{ bar} \times \text{liter}$ (below).

is close to) the number of neon atoms per m^3 injected in the AUG plasma volume (14 m^3) in shots 30440-30442 with two valves. In the pulses n. 30438 and n. 30439, the LFS and the HFS valve were fired one at a time, reducing to half the gas quantity injected.

- *Changing gas type.* Four ohmic discharges were terminated by injection of D_2 and He gas with the LFS-S13 valve, in amounts corresponding to 50 % and 25 % of the quoted maximum. These discharges have the longest (within this experiment) pre-TQ phases within the dedicated set.

- *Safety factor scan.* The reference pulse (n. 30440) was modified by changing both plasma current (from 1 to 0.8 MA) and toroidal magnetic field (from 2.5 T to 1.5 T and

shot n.	gas type	quantity [bar × l]	valves	I_p [MA]	$E_{th}(t_{trig})$ [MJ]	$E_{th}(t_{TQ})$ [MJ]	q_{95} [adim]	Δt_{pre-TQ} [ms]
30438	Ne	0.85	HFS-S4	1.0	0.44	0.22	4.3	2.4
30439	Ne	0.85	LFS-S13	1.0	0.47	0.26	4.3	1.5
30440	Ne	1.70	S4 + S13	1.0	0.53	0.26	4.3	1.7
30441	Ne	1.70	S4 + S13	1.0	0.09	0.1	4.0	1.4
30442	Ne	1.70	S4 + S13	1.0	0.73	0.45	4.2	1.55
30443	D ₂	0.42	LFS-S13	1.0	0.05	> 0.05	4.5	3.1
30444	He	0.42	LFS-S13	1.0	0.14	> 0.14	4.3	3.0
30752	Ne	1.70	S4 + S13	0.8	0.35	0.15	3.1	1.5
30754	Ne	1.70	S4 + S13	0.8	0.33	0.20	5.7	1.7
31025	D ₂	0.42	LFS-S13	1.0	0.18	0.12	4.5	3.5
31026	D ₂	0.85	LFS-S13	1.0	0.15	0.10	4.5	2.8

Table 1. Dedicated discharges for modeling.

2.7 T respectively) in order to obtain the largest possible variation of q_{95} (which resulted to be 3.1 and 5.7 respectively). Contrary to any expectation, the pre-TQ duration did not vary much with q_{95} .

2.3. Relevant diagnostics

2.3.1. Diode bolometers. AUG is equipped with several AXUV diode arrays [12] in sector 5 and 13, displaced toroidally by an angle $\Delta\Phi = \pi$ from each other, which allow the reconstruction of the radiation intensity emitted at these toroidal locations. Sector 5 hosts several photodiodes, which allow a rough tomographic reconstruction of the radiation; sector 13 is equipped with a single vertical photodiode. The geometry of the vertical photodiodes in sector 5 and 13 is (very similar at both toroidal location) shows in figure 3 (left).

The AXUV diodes can be calibrated, i.e. used to infer radiated power, only at temperatures > 1 keV. At lower temperatures they cannot provide a quantitative measurement of the radiated power, since their responsivity (i.e. the diode current per photon energy absorbed) depends on the photon energy, which is not known, and decreases with it. Synchronized bolometric measurements would be needed for the calibration. For example, we observe that during the current quench a significant amount of magnetic energy is dissipated and radiated, but the diodes barely detect any radiation. Nevertheless the diode arrays, with their high time resolution, detect what is interpreted as the propagation of the cold front into the plasma, show filamentary structures, the redistribution of the gas within the plasma section during the current quench and give information on the toroidal asymmetry of the radiated power, i.e. provide precious

observations on the evolution of the gas-plasma interaction.

AUG is also equipped with several arrays of foil bolometers in sector 5, i.e. close to the HFS valve. The finest time resolution of the AUG bolometers is 1 ms (i.e. they measure much slower than diodes) but, in principle, they have the advantage of being absolutely calibrated. In the past, the radiated energy measured by this diagnostic during the disruption was reasonable and of the order of 70-90 % of the total plasma energy. Correct bolometric measurements are not available for the dedicated set of discharges under investigation; therefore it is impossible at the moment to discuss power/energy balance during plasma termination, along with all the details of energy dissipation in plasma and deposition on the PFCs.

2.3.2. CO₂ interferometer chords. Measurements of the density evolution during and after MGI are crucial for the interpretation of the plasma dynamics. On AUG, the CO₂ laser interferometer (see right side of fig. 3 and ref. [13] for details) can provide measurements of the line integrated density along two vertical chords in one toroidal sector (sector 11) after MGI. Since ASTRA-STRAHL does not contain the physical models of the processes determining the fuelling efficiency (of the order of 30 %), but employs a simple penetration/ionization model for the injected neutral gas, the density measured during the current quench will be used to set (decrease) in the simulation the neutral gas source, in order to take into account particle losses which cannot be computed.

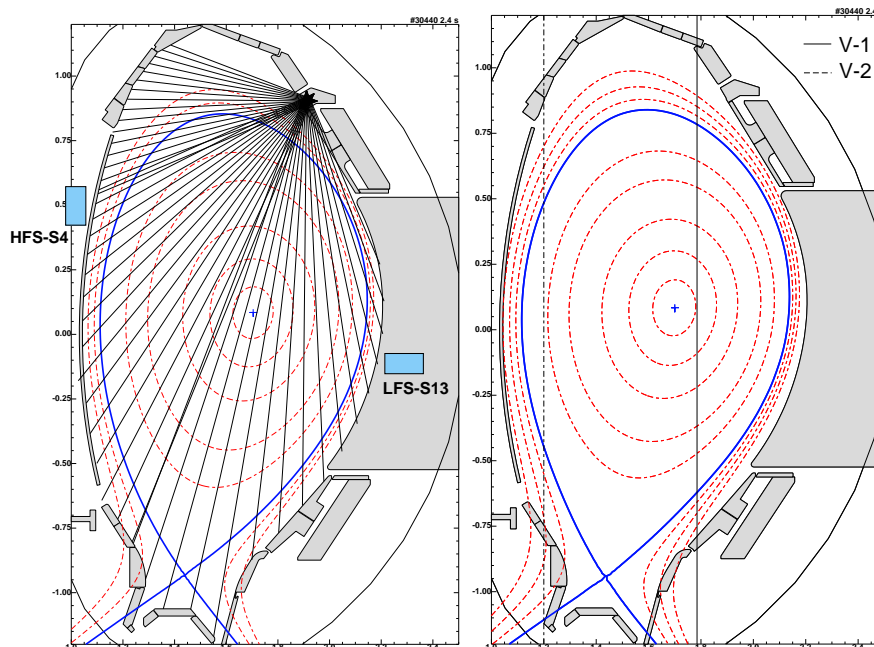


Figure 3. Geometry of the AUXV vertical photodiode(s) in sec. 13 and sec. 4 (left). The two CO₂ chords located in sec. 11 (right).

2.3.3. Plasma parameter profiles. Profiles of the density and of the electron temperature are the result of an integrated data analysis (IDA, ref. [14]) of several diagnostics based on Bayesian probability theory; the ion temperature profiles are from charge exchange. These profiles are available only for the target plasma; as soon as the gas reaches the plasma edge, most of the kinetic diagnostic (except the CO₂) measurements become invalid. The current density is not measured on AUG but it is calculated by ASTRA self-consistently with the measured electron temperature and a given form of the resistivity. The presence of small (width still to be measured) NTMs in some of the discharges allows the localization of rational flux surfaces and the re-computation of an equilibrium subject to these flux surfaces being constrained at the observed spatial location. Such an improved equilibrium can be imported in ASTRA for simulations but this was not done in this work.

2.4. Experimental measurements

2.4.1. Duration of the pre-thermal quench phase. The pre-TQ is defined as the time between the arrival of the gas at the plasma edge (seen by the AXUV diodes in front of the valve) and the start of the core thermal energy collapse (i.e. drop of the emission measured by central SXR cameras). Figure 4 shows time traces of this phase for the pulse 30440. The valve was triggered at $t = 2.496$ s in this plasma discharge; the gas arrived at the plasma edge 0.7 ms later, as seen by the diodes in front of the valves (fig. 4 (e)). The Mirnov coils show the development of magnetic fluctuations and then low m/n modes starting at 0.3 ms after the gas arrival (fig. 4 (c) and (d)); this MHD activity causes the thermal quench at $t = 2.4985$, i.e the collapse of the central SXR channels and the beginning of the current quench (fig. 4 (f) and (a)).

The duration of the pre-TQ phase is reported in table 1 for the different discharges. This phase is weakly dependent on E_{th} , gas quantity and q_{95} , and more strongly dependent on injection side and on gas type; these data confirm previous AUG results [15] obtained injecting similar gas quantities.

Nevertheless, it is known that at lower - of one order of magnitude - amounts of injected gas, the pre-TQ phase duration depends significantly on plasma thermal energy (figure 5) and gas amount [1]. In addition, the presence of rotating or locked modes can shorten the pre-TQ [16] and can be the reason for the scatter seen in figure 5, which contains discharges with and without modes. Since the gas amount, which will result in an optimized mitigation of the ITER plasmas, is not known at the moment, a discussion of the parametric dependence of Δt_{pre-TQ} on plasma and gas parameters found in the ASTRA-STRAHL simulations at a lower amount of injected gas will be included in Part II of this report.

It is worth noting that the lack of dependence of Δt_{pre-TQ} on E_{th} and gas quantity, in the dedicated experiment under analysis, is not intuitive.

According to the physical picture that we have in mind, the impurity ions, which cause local radiative temperature collapse, are transported into the plasma up to the

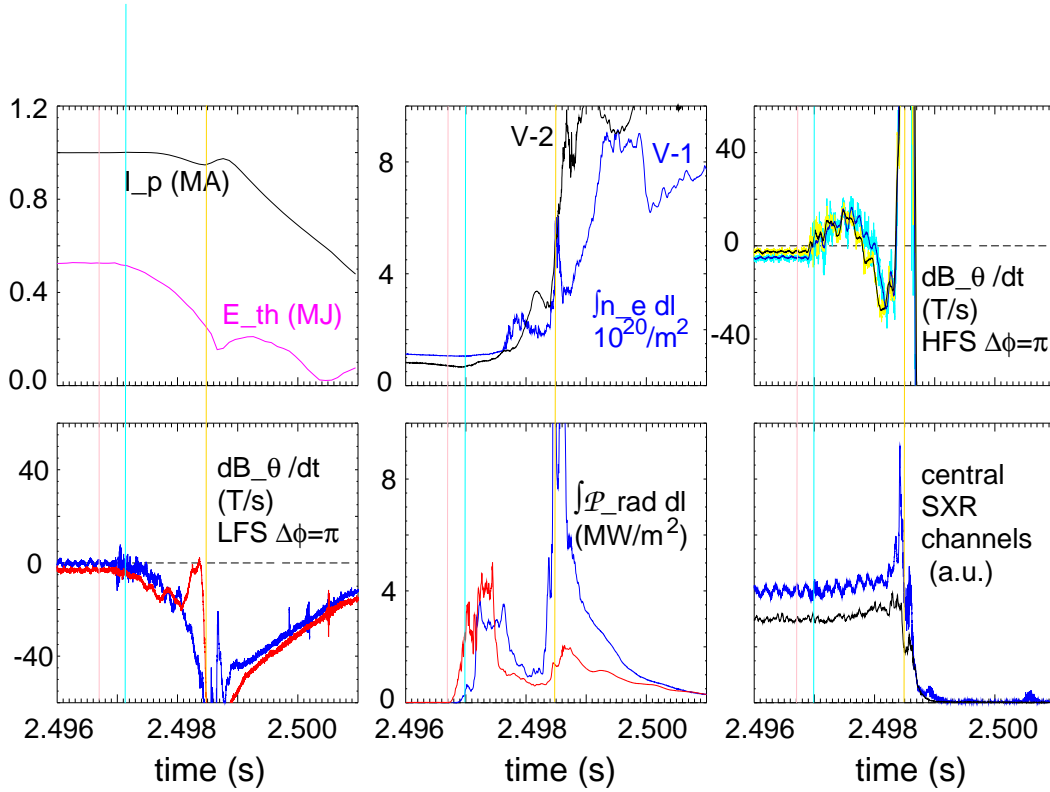


Figure 4. Time traces of plasma parameters during the pre-TQ (pulse 30440): (a) plasma current (I_p) and thermal energy (E_{th}); (b) line integrated density along the V-1 and V-2 CO₂ interferometer cords; (c) signals of two Mirnov coils, located on the HFS at the torus midplane, displaced toroidally of an angle $\Delta\Phi = \pi$; (d) signals of two Mirnov coils, located on the LFS at the torus midplane, displaced toroidally of $\Delta\Phi = \pi$; (e) line integrated radiation measured by the two diodes viewing the foot prints - two valves - of the incoming gas at the plasma edge; (f) two central SXR channels

$q=2$ surface, causes the growth of the $m=2, n=1$ mode (and other harmonics) which then triggers the thermal quench. As it will be shown later in the simulation results, behind the cooling front, at which the impurity ions produce most of the radiation, the neutral gas is mostly ionized and the ionization balance leads to low- Z charge states ($Z \sim 1-2$). However, due to a combination of low temperature and low charge state, neutrals can still penetrate up to the cooling front, thus allowing the average penetration speed to be faster than the transport time scale. The cooling of the region between plasma edge and $q=2$ implies that

$$\Delta t_{pre-TQ} \propto E_{th}(q > 2)/P_{rad} \propto E_{th}/[f_Z(T_e) n_e^2] \quad (1)$$

where the approximation $n_Z \approx n_e$ has been used as the electrons generated by MGI gas ionization far exceeds the background electron density.

Although E_{th} and n_e have been varied independently from each other by one order of magnitude (this experiment and [15]), they do not influence the pre-TQ duration

as strongly as expected. Moreover, the observation that Δt_{pre-TQ} does not depend on E_{th} implies that $P_{rad} \propto E_{th}$ and this is actually observed in the experiment. Figure 6 shows the linear dependence between the radiated power measured by the diode arrays, integrated during the pre-TQ phase and averaged between sector 13 and sector 5, and the target plasma energy. Correct foil bolometer measurements, necessary for the absolute calibration of the diodes, were not available for these discharges, and therefore the vertical axis is in a.u..

2.4.2. Radiation front penetration. Typical contour plots of the radiation emitted by the plasma during the whole gas-plasma interaction, as seen by the AXUV vertical cameras, are shown in figure 7. At about 2.497 s, channel 5 in sector 13 and channel 28 in sector 5 start seeing the gas radiating while interacting with the plasma in front of the valves. The position of the maximum radiation moves towards higher (figure 8) and lower channel numbers respectively, i.e. towards the plasma centre, leaving behind a non-radiative (because cold) plasma. In sector 13, filaments are seen detaching from the radiation front and rotating in the ion diamagnetic drift direction. At 2.4982 s the radiation starts spreading rapidly over the whole plasma; this is interpreted as a rapid redistribution of the impurities over the whole plasma because of a transient increase of diffusivity and temperature. This is the thermal quench phase of the disruption: the still hot plasma core loses its confinement and the resulting heat flux, directed outwards, heats the impurities; convection caused by strong MHD activity is probably also playing an important role in mixing the impurities with the background plasma.

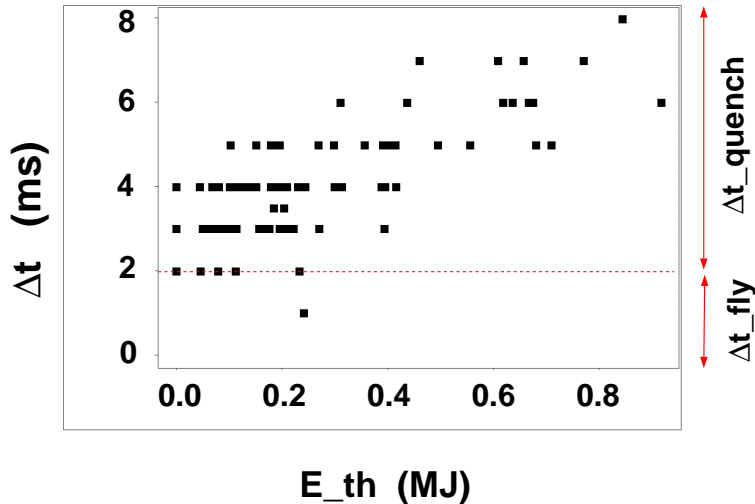


Figure 5. Delay between trigger and thermal quench onset as function of thermal energy [1].

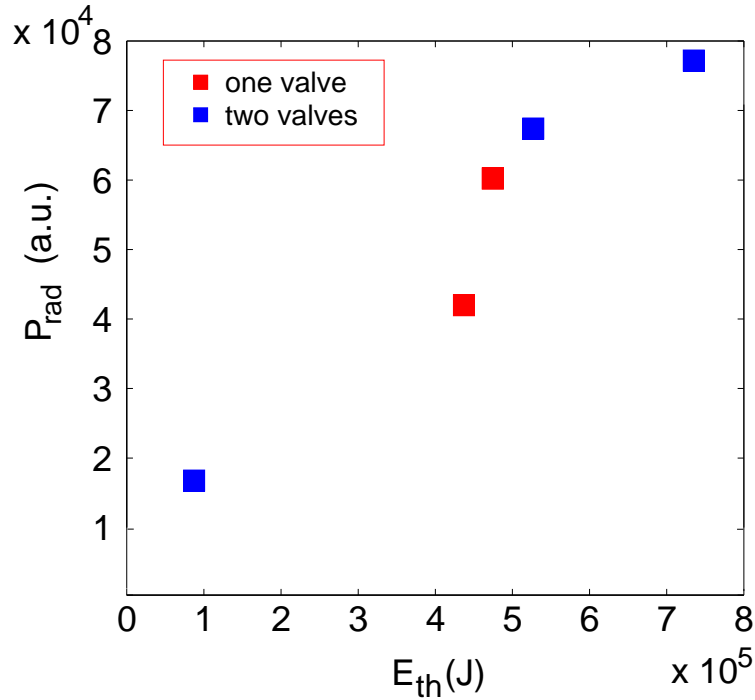


Figure 6. Radiated power measured by the diode arrays during the pre-TQ phase versus the target plasma energy.

3. Model description

Modeling of the pre-TQ phase, described in the previous sections, is performed with the ASTRA transport code [17, 18], coupled to the 2D equilibrium code SPIDER [19] and the 1D impurity transport code STRAHL [20]. The transport models used for the electron and ion temperatures, electron density, and impurity densities, are described below.

This modeling is 1D in nature, as such it has to be taken with care which physics is actually relevant also for the more realistic 3D case. A-posteriori this can be done, but in addition 1D modeling already provides very useful indications on some of the observed scalings, and on their possible physics origin. This would give confidence that a 1D model could project to a future machine, provided the missing physics (3D vs 1D) is still estimated to be marginal, at least up to some point (in time or space).

The observed dependency of the pre-TQ phase on several plasma parameters (stored energy, safety factor, gas influx, gas type) is investigated via modeling, and it will be shown below that some of the dependencies are correctly captured within the 1D framework. The scenarios to be modeled have been presented in the previous sections. In particular the discharge #30440 is used for parametric studies. Further discharges are used to explore dependencies on plasma energy, safety factor q , and gas type. Details on the simulation model are given below.

Transport equations are advanced according to the prescription given in the two

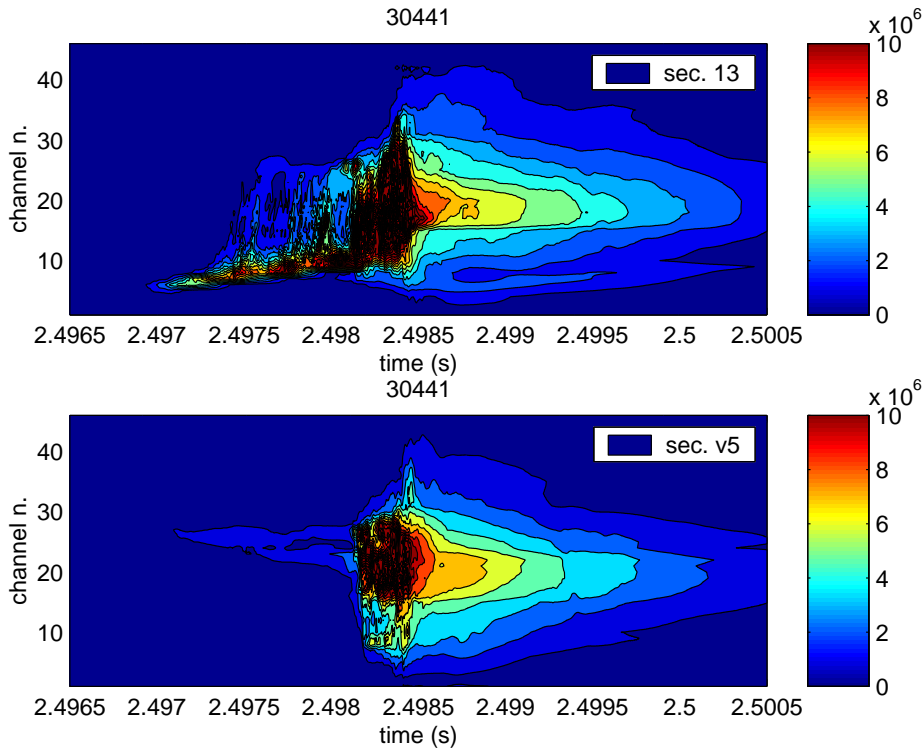


Figure 7. Contour plot of the radiative emission as measured by the AUXV vertical cameras in sector 13 and sector 5.

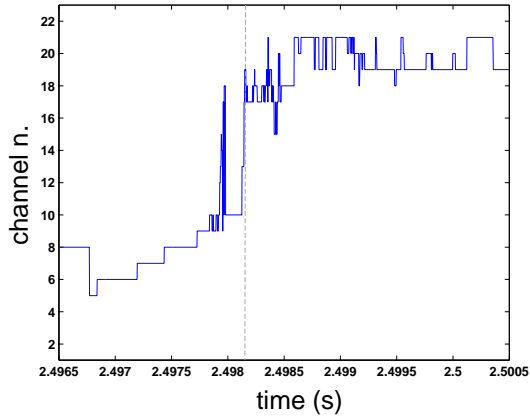


Figure 8. Position of the max radiation (channel number) as seen by the AXUV vertical camera in sector 13 (shot 30441). The $q = 2$ surface intercepts chords 8-9 at the vertical height of the gas valve LFS-S13. The vertical dashed line approximately indicates the time of the thermal quench.

codes ASTRA and STRAHL, i.e. ASTRA advances electron and ion temperature, deuterium density, and plasma current profile. STRAHL advances profiles of impurity densities per charge state. The boundary conditions in ASTRA are set at $\rho_n = 1$ (with $\rho_n = \sqrt{\Phi/\Phi_b}$ the normalized toroidal magnetic flux coordinate) for every profile. The current profile is evolved assuming neoclassical resistivity and imposing conservation

of the total plasma current. No additional current is driven apart from the Ohmic and the bootstrap currents. The boundary conditions in STRAHL are described in the STRAHL user manual [20]. However STRAHL is used practically to compute neoclassical transport and impurity profiles in the plasma core, while the Scrap-Off-Layer (SOL) part is just a region where impurity sources are set.

3.1. Core T_e and T_i modeling

The evolution of the electron and ion temperature, T_e and T_i , is obtained by assuming the following diffusivities:

$$\chi_{e,i} = \chi_{e,i}^{\text{PB}} + \chi_{e,i}^{\text{NEO}} \quad (+\chi_{e,i}^{\text{MHD}}) \quad (2)$$

where $\chi_{e,i}^{\text{PB}}$ is the power balance diffusivity, based on pre-MGI profiles, and kept constant during the pre-TQ phase. $\chi_{e,i}^{\text{NEO}}$ is the neoclassical heat diffusivity, which is negligible in the steady-state phase before the gas injection, but which can become the dominant transport channel during the MGI phase (aside from MHD). The latter additional contribution, $\chi_{e,i}^{\text{MHD}}$, can be used as a "scan" parameter to test the sensitivity and to try to mock-up experimentally observed modes.

As boundary condition for the temperatures, one can choose to either fix its value at the plasma separatrix, or to fix a constant pressure. In the simulations presented later, the latter choice is used, so that $T_e = p_{e,0}/n_e$ and $T_i = p_{i,0}/n_i$, where $p_{e,0}, p_{i,0}$ are the initial electron and ion pressures at the separatrix.

As regards the sources, both ECRH and NBI power deposition profiles are computed before the MGI and then kept fixed to provide the background heating. Their levels is in the order of 2–5 MW and as such it is anyway negligible to the radiated power in the MGI phase. The Ohmic power is consistently computed, and the equipartition power between electrons and ions is also included. No other sources/sink are considered, except line radiation as a sink on the electron species. Charge exchange losses are ignored, while ionization/recombination losses are included together with line radiation.

3.2. Core n_e and n_Z modeling

Modeling of the electron density n_e and of the various impurity density profiles n_Z is performed as well. The electron density follows from quasi-neutrality: $n_e = n_D + Z n_Z$, with Z being the average impurity charge. The deuterium density n_D is kept fixed at the pre-MGI profile.

For the impurities, the anomalous part of the diffusion is chosen as $D_Z \propto \chi_e + \chi_i$. This choice of D_Z , which may seem arbitrary, is reasonable with respect to estimate from theory. Moreover its impact on the quantitative evolution of the cooling front is minimal, as the main player are the neutral gas penetration, radiation cooling, and collisional transport that takes over at the highly collisional cooling front. MHD-driven transport can also dominate, but is not accounted for in the present modeling.

The neoclassical contribution is computed in STRAHL using the NEOART module [21]. The impurity anomalous convection velocity is set to 0. The neoclassical contribution to the impurity convection is computed with NEOART. No neutral impurity source is assumed inside the separatrix. Note that no rotation effects are considered for the impurities. This could be justified by the fact that the neutrals would brake the plasma strongly in the same region in which they are ionized.

3.3. SOL model

The Scrape-Off-Layer is not modeled in ASTRA, but it is used in STRAHL for the impurity propagation to the separatrix. There, all diffusivities are assumed to be 0.5 m²/s in the SOL.

The gas source Φ in STRAHL is set 2 cm outside of the last closed flux surface (LCFS) and given in particles per second [p/s]. This means that the impurity neutral boundary condition at the LCFS+2 cm is computed from the formula: $n_{n,b} = \frac{\Phi}{4\pi^2 R a v_n}$, where v_n is the neutral thermal velocity. Losses and ionizations in the 2 cm of SOL are computed. However they result in a negligible reduction of the neutrals at the LCFS. In the experiment, the actual flux reaching the plasma boundary will be lower due to real SOL losses as, e.g. ionization and parallel transport. As such, the max value used in the simulation corresponds to 1/3 of the experimental flux and is probably closer to the real flux entering in the plasma.

The impurity neutrals penetration model from the separatrix into the plasma core is described below. A continuity equation (in toroidal geometry) is solved: $\nabla \cdot (n_Z \mathbf{v}_Z) = S_Z$ where n_Z is the neutral density of impurity Z , v_Z is the impurity propagation speed (equal to thermal speed), and S_Z is the sum of sink (ionization) and source (recombination). Note that the impurities are assumed as 'instantaneously' propagated, i.e. the continuity equation has no time derivative. This means that it has to be checked a-posteriori that the cold front propagation speed is lower than the neutral sound speed for the simulation to have physical meaning. Otherwise the sound speed would be the upper limit. As it will be shown later, in all studied cases it is found that the propagation speed is substantially below the neutral thermal speed (estimated at ~ 350 m/s at ambient temperature for neon).

In addition to discharge modeling, sensitivity scans have been carried out to assess the role of: 1) gas influx, 2) plasma energy and safety factor, 3) local and global transport. These are the most relevant elements that should, via comparison to experiments, give a deeper understanding of the physics of the pre-TQ and appropriate extrapolation to future devices.

4. Simulation results

Several modeling results are reported in this section. For the following simulations the ASTRA radial grid consists of 321 equispaced points ($dx = 2$ mm), while the time step

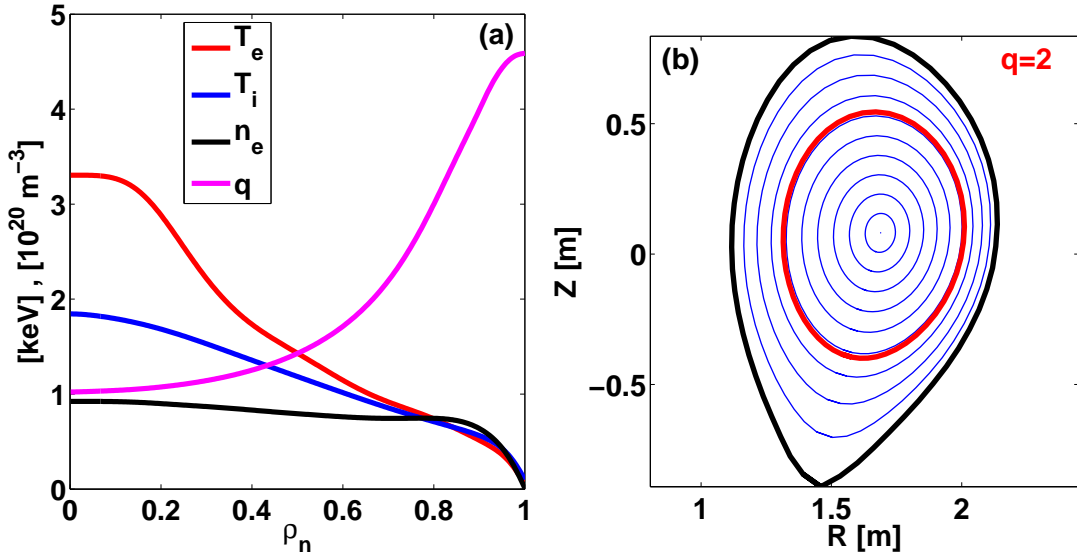


Figure 9. a) Temperatures (T_e, T_i), electron density, and safety factor (q) profiles before the MGI, for #30440; b) equilibrium flux surfaces with $q = 2$ evidenced.

used is $dt = 1$ [μs].

4.1. Reference scenario

Discharge #30440 is modeled with the ASTRA-SPIDER-STRAHL codes suite. The target plasma is a standard H-mode at 1 MA of current and 2.5 T of magnetic field. Neon (Ne) is injected by the HFS and LFS valves at $t \approx 2.496$ s. A gas flux scan around the nominal value is performed to assess the penetration time, and matching with measurements. The time evolution of the injected gas flow rate in [p/s], normalized to the maximum value, has been shown in figure 2(bottom). The maximum value is then scanned in the interval $[0.09, \dots, 4.6]10^{24}$ [p/s]. The nominal max value of the flux in the experiment is $\sim 1.5 \cdot 10^{25}$ [p/s] for a gas pressure in the valve of 20 bar. As discussed in the previous subsection, the max value used in the simulation, $\sim 4.6 \cdot 10^{24}$ [p/s], is about 1/3 of the experimental nominal value.

The initial temperature, density, and safety factor profiles before the MGI are shown in figure 9(a). The flux surfaces shape are shown in figure 9(b), with the $q = 2$ surface evidenced.

After the opening of the valve and the gas reached the hot plasma, electrons and Ne ions are generated through ionizations and the rapidly increasing radiation collapses the T_e profile starting from the edge, and moving inwards. The characterization of the penetration of the "cold front" is now introduced. The following identity is employed:

$$V_{T_0} = - \left[\frac{1}{\langle \nabla \rho \rangle \frac{\partial T_e}{\partial \rho}} \frac{\partial T_e}{\partial t} \right]_{T_e=T_0} \quad (3)$$

to compute the flux-surface-averaged radial velocity V_{T_0} of the displacement of surfaces at constant $T_e = T_0$. This formula is used to reconstruct the velocity V_{T_0} from the simulation and compare it to estimates based on the simulated radiated power (see below). The value of the temperature of the reference surface is chosen as $T_0 = 5$ [eV] (notice that this value could change depending on the simulation result, as in some cases the temperature drop is not as strong). V_{T_0} is only a proxy for the cold front propagation speed. In reality the cold front has a moderate radial extent. Its width depends on the balance between radiation and diffusion. Notice that, for a moderate-to-high-Z impurity as Ne, one expects the dominant balance $\frac{\partial T_e}{\partial t} \sim -P_{\text{rad}}/n_e$. Thus one obtains $V_{T_0} \propto P_{\text{rad}}$. It will be shown that this is in fact confirmed by the simulation results. Note that one can neglect the term $T_e \frac{\partial \log n_e}{\partial t}$ as compared to the term proportional to the radiated power. This is of course a good approximation only for strongly radiating impurities.

4.1.1. Profile evolution for maximum flux case The evolution of various profiles are shown in figure 10(a,b,c,d), for the maximum value of the Ne flow rate of $4.6 \cdot 10^{24}$ [p/s]. It can be seen in figure 10(a) that both T_e and T_i are being eroded by the penetrating gas due to the large localized radiated power, figure 10(d). The radiated power dissipates T_e , while T_i collapses due to the equipartition power that increases enormously in the high-collisionality region, forcing $T_i \rightarrow T_e$. The region inside the cold front is unaffected on this time scale.

The n_e and n_Z profiles in figure 10(b) show the ionization front propagating more and more into the core plasma. As the edge region becomes cold, the ionization rate there is reduced, while recombination becomes dominant. This explains the decay of the n_e profile towards the edge.

Finally, in figure 10(c), the parallel current density J_{\parallel} profile is shown. As expected, the current column shrinks. The spiky feature is such as to maintain the total plasma current fixed to the experimental value, since in the cold region, the current is almost zero. One could then hypothesize that the current/pressure gradients will lead to some strong, non-linear, localized MHD activity, as well as global MHD driven by modified equilibrium; however the latter mechanisms are not included in the model but need to be demonstrated with actual MHD codes.

4.1.2. Gas flow rate scan Based on the same case #30440, a scan in gas flow rate is performed. The location of the flux surface with at $T_e = 5$ eV, which is a proxy for the cold front location, is then found at each time step. The penetration of this front as a function of time and gas flow rate is shown in figure 11(a). These results show that the time of arrival of the cold front near the $q = 2$ surface decreases with increasing gas influx.

To have an idea on how the cold front traveling speed changes with flow rate, the time trace of V_{T_0} for the different fluxes is shown in figure 11(b). The speed is expressed

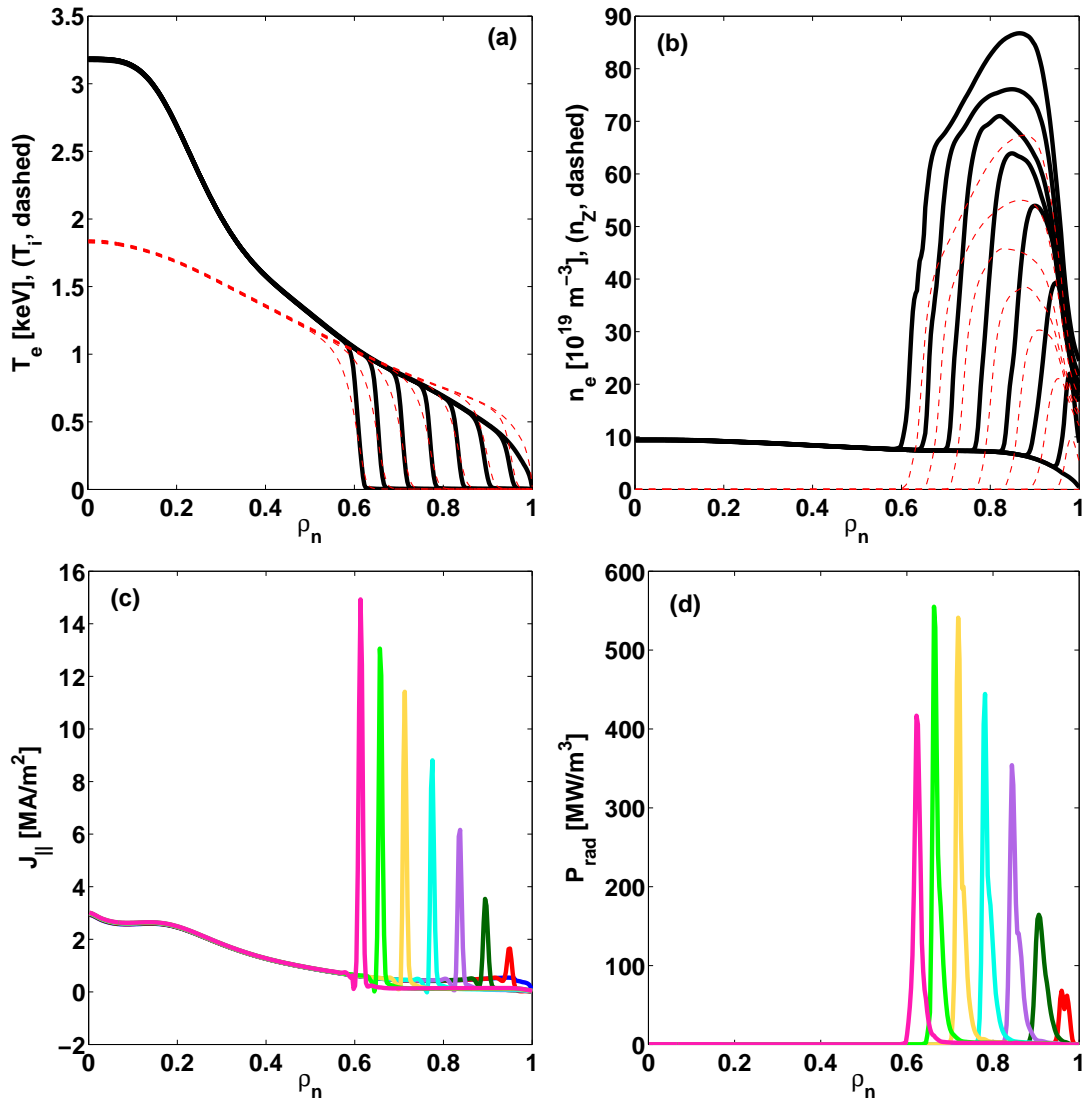


Figure 10. a) Evolution of T_e (solid) and T_i (dashed) profiles during pre-TQ phase; b) evolution of n_e (solid) and n_Z (dashed); c) parallel current; d) line radiation profiles. Profiles are equispaced in time by 0.2 ms (i.e. last profile is at 1.6 ms after initiation of gas injection).

in [cm/ms], as it gives a rough idea on how much time the front would take to penetrate fully into the plasma (50 cm for AUG, and ~ 15 cm to the $q = 2$ surface). The relation between the penetration speed and the radiated power can be seen in figure 12(a), where the time traces of the total radiated power are plotted, with the same color code as in figure 11(a,b). The two sets of time traces are strikingly similar, which supports the hypothesis that the penetration speed is dominated by the radiation process. The details of the physics behind this relation and the time evolution of P_{rad} will be presented in the next sections.

In figure 13, the time traces of the plasma energy, W (left plot), and its time

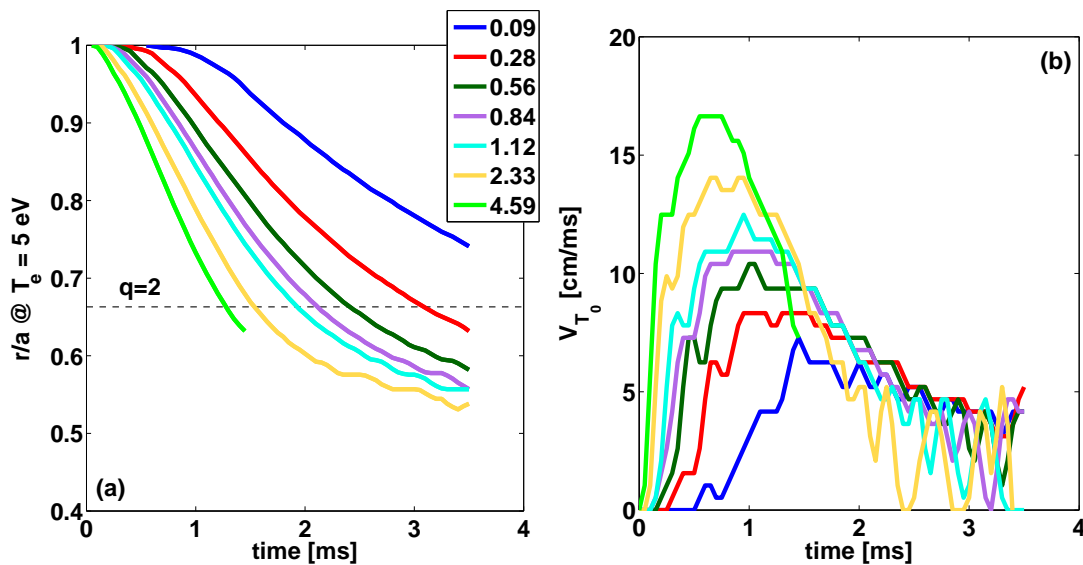


Figure 11. a) Time evolution of the location of the innermost $T_e = 5$ eV flux surface. In legend: values of the max gas flow rate in units of 10^{24} p/s; b) time trace of the cold front propagation velocity V_{T_0} .

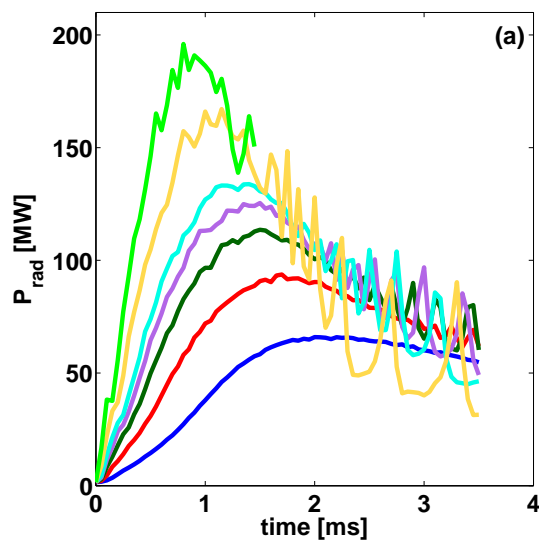


Figure 12. a) Time evolution of the total radiated power in the plasma core (same color coding as previous figures).

derivative dW/dt (right plot) are shown, and simulation results and experimental measurements (EXP) are compared. It is clear that the energy removal rate (loss power via radiation) decreases with time, indicating less efficiency as the cold front penetrates into the core. This is partly due to the gas-rate slope, that has a maximum of injected gas at around 1.5–2 ms; however this effect is mostly due to the loss of efficiency in neutral penetration when the cold region gets larger. To recover the experimental curve, some kind of "acceleration mechanism" should be invoked, most probably driven

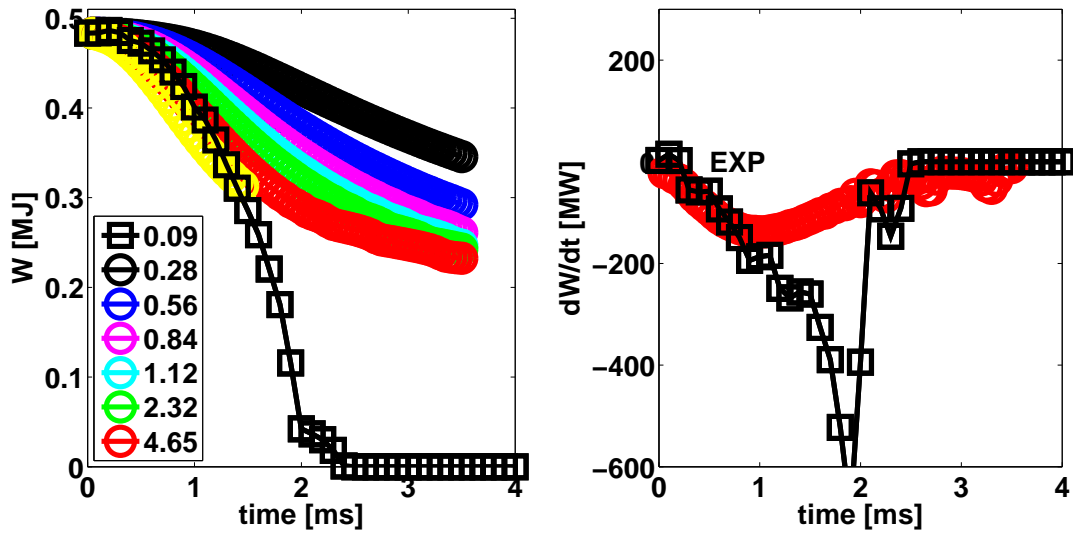


Figure 13. Left plot: Time trace of the plasma energy W [MJ] from equilibrium reconstruction (EXP), and from simulations (colored lines). Gas-rate in 10^{24} [p/s] is indicated in the legend. Right plot: Time trace of the transient loss power dW/dt [MW], where only the case with gas-rate of 2.32 (red) is shown against the experiment.

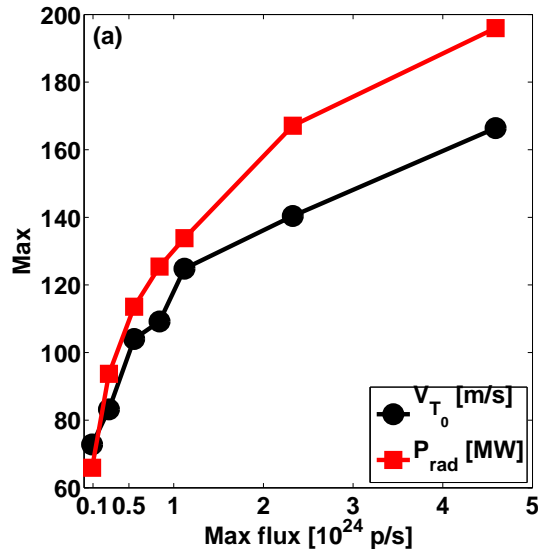


Figure 14. a) Max penetration speed (circles) and max P_{rad} (squares) versus max injected gas flux.

by underlying transport (i.e. non-linear MHD).

Finally, the relation between the injected gas flux and the maximum penetration speed/radiation is shown in figure 14. A good fit in this range of fluxes is obtained as: $\max(P_{rad}) \sim [\max(\Phi)]^{0.275}$ (where Φ is the input gas flux in [p/s]). This shows that the response after the gas-plasma interaction is not at all linear in the input gas flux, which

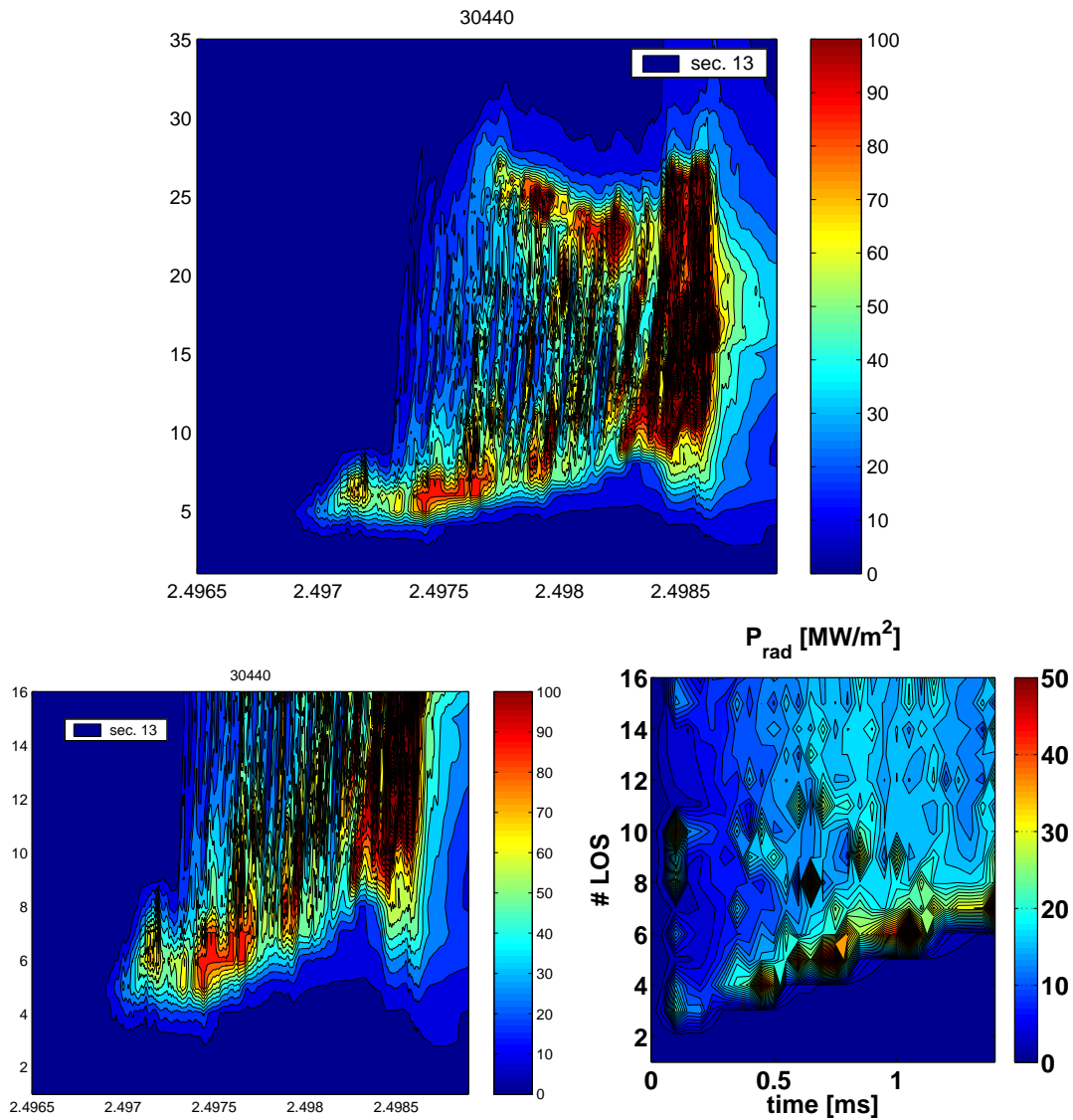


Figure 15. Contour plots of the bolometer LOS radiated power in MW/m^2 (top plot is full LOS from experimental measurements, bottom-left plot is a zoom on LFS-oriented LOS). Bottom-right plot is simulation result. For this case, the max flux used is $4.6 \cdot 10^{24}$ [p/s].

is also observed experimentally.

4.1.3. Comparison with the diode bolometer line-of-sights. A synthetic diode bolometer diagnostic has been implemented in ASTRA. Each LOS is assumed to be infinitely thin. It produces the signal observed by the real diode bolometer line-of-sights as line-integrated radiation.

A 2D contour plot of the measured line integrated radiation (LOS from LFS to HFS) is shown in figure 15(top plot). On the bottom plots, the measurements are zoomed on the LFS (LOS from #1 to #16), while in (a) the simulation result is shown.

The simulated contour plot shows comparable behavior, i.e. the motion of the peak radiation from the lower to higher camera number as the cold front moves inwards into the plasma (or in real space from LFS towards the plasma center). Notice that the measurements show a marked asymmetry between LFS and HFS, also with some filamentary structures propagating across the LOS, while the simulated contour plot is symmetric (not shown), and the filaments are absent. In fact, in the simulation, that assumes toroidal/poloidal symmetry, line-of-sights on the HFS that should not see any radiation, actually see it.

In figure 16 the "profile" along the LOS is shown from the measurements (top plot), and from the simulations in bottom plot. Here the LFS-HFS asymmetry in the measurement against the symmetry in the simulation can be observed. Also notice that the measurements seems to display "acceleration" and "spreading" as the front proceeds, while in the simulation the front looks self-similar in shape. The amplitude evolution instead is rather similar between measurement and simulation.

4.1.4. Explanation of the gas rate dependence of the penetration time. For highly radiating impurities like Ne, one can estimate formula (3) as $V_{T_0} \sim \frac{P_{\text{rad}}}{n_e \partial_r T_e} \sim L_Z n_Z a / \langle T_e \rangle$, with L_Z and n_Z being the impurity cooling rate and the density respectively, whereas $a, \langle T_e \rangle$ are the minor radius and the average electron temperature. For the same discharge, a variation in gas rate corresponds to a variation of n_Z . One could naively think that the average production of n_Z should depend linearly on the gas rate. Actually, a more accurate analysis on the simplest model reveals already that $n_Z \sim \Phi^{0.5}$, where Φ is the gas-rate in [p/s]. The reason for the square-root dependence is that the minimal system consists of two coupled first-order time-dependent equations, one for n_Z and one for T_e , leading to a second-order time dependence that is linear in Φ . Straightforward integration leads to the square-root dependence. Nevertheless, the simulations show that $n_Z \sim \Phi^{0.25-0.3}$. To visualize this behavior, in figure 17 the time evolution of the ratio of Ne ions n_Z and neutrals over the gas-rate, at the cold front position is shown.

One can see that, as the gas-rate is increased, the two ratios decrease, indicating that both the process of neutral penetration and ionization becomes less efficient at higher flux. The reason is that the cold front is very localized, and the cold region behind is basically a sink for the incoming neutrals which are ionized there but do not contribute to the radiation at the cold front. Note that here the transport of neutrals is not addressed, as for example done in [22] or [5], where they considered either the CX friction between neutrals and ions, [22], leading to a slowing down of the neutral penetration, or the effect of secondary neutral generation through recombination, [5]. In the present model, neutrals represent the source of the ionization stage +1 of Ne, but there is not recombination, nor secondary neutral generation, nor CX losses. The latter could be more relevant for D however in terms of power loss channel.

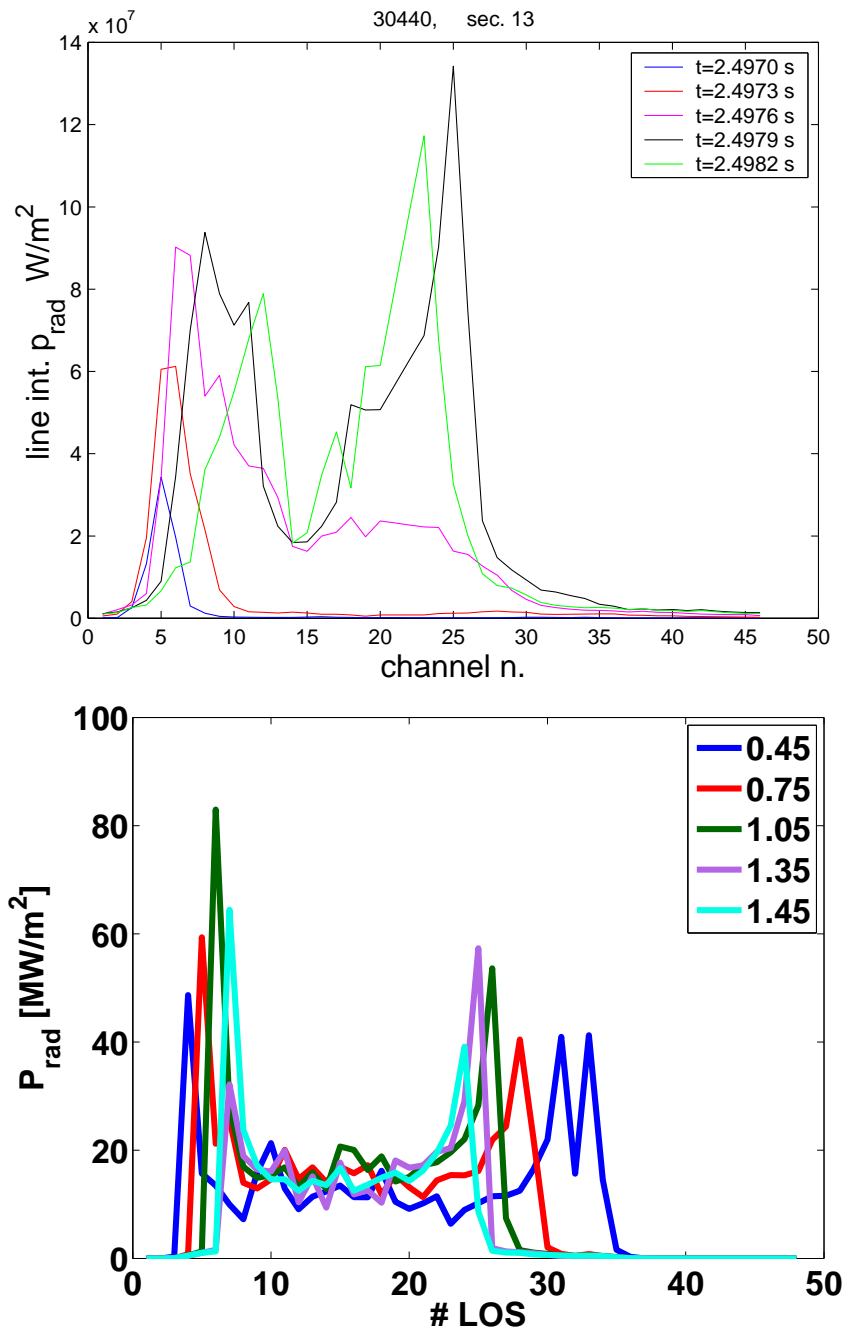


Figure 16. Top plot: LOS-resolved profiles of measured line-integrated radiated power in MW/m^2 for different time slices (in legend) during the MGI. Bottom plot: simulation results, with time slices (in ms) shown in legend.

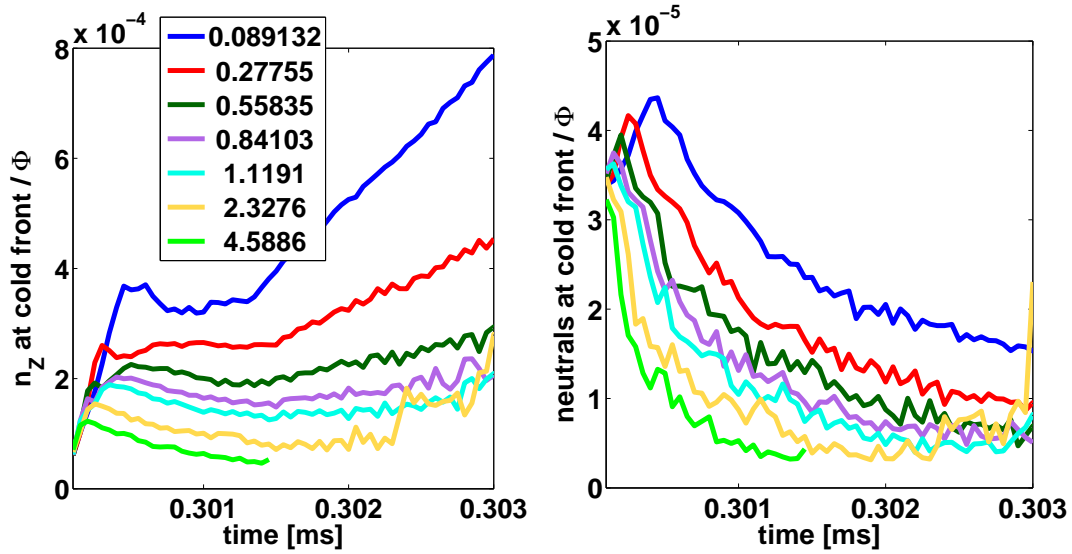


Figure 17. Time trace of (left plot) ratio of Ne ion density n_z over gas-rate (flux), at the cold front position, plotted for different values of the gas-rate Φ (in legend, units of 10^{24} p/s). (right plot) ratio of neutral Ne density at the cold front position over gas-rate.

4.2. Dependence of the pre-TQ time on the value of the safety factor

Two discharges provide a scan in q_{95} for very similar plasma conditions (total plasma current is constant, i.e. the field is varied); the two values of q_{95} are 3.1 (#30752) and 5.7 (#30754) respectively. The electron density in the second discharge is $\sim 20\%$ lower than in the former, while the temperatures are the same. The energy outside of the $q = 2$ surface is respectively ~ 40 kJ in the low q_{95} case and ~ 70 kJ in the high q_{95} case.

Three values of the gas-rate are used, and the results of this double scan are shown in figure 18. The cold front position in normalized coordinate is shown as a function of time. The two values of q_{95} are depicted in black and red, while the different line types refer to different gas-rates. Also the position of the $q = 2$ surfaces are computed and displayed as horizontal lines.

The simulation results show that a significant delay between the time that the cold front takes to reach the $q = 2$ exists between the two discharges. This is in contrast with the experiment, where the higher q_{95} case has a pre-TQ time not very much different than the case at lower q_{95} . This observation could be understood if the cold front accelerated as it reached deeper into the plasma. This acceleration would be consistent with what has been discussed for the energy time trace in previous sections, see figure 13. Another possibility is that the mode growth rate sets a minimum to the pre-TQ time duration in the low q_{95} case, however this would also imply that the 1D model gets the timescale right only by chance. Note that the MHD itself could be different in the two q_{95} cases.

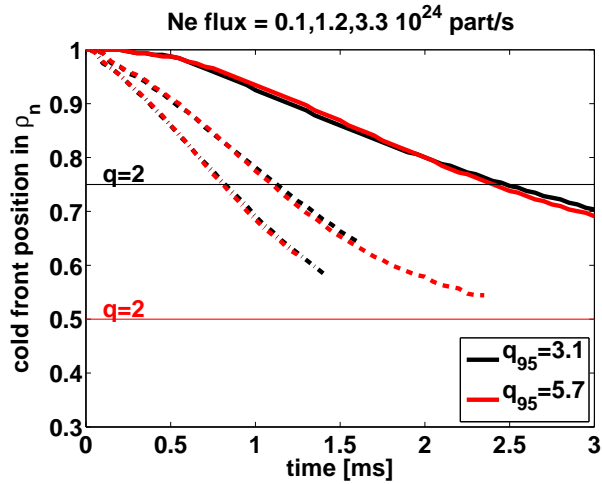


Figure 18. Time trace of the cold front position for different gas rates (solid: 0.1, dashed: 1.2, dot-dashed: 3.3 all in 10^{24} [p/s]) and for different safety factor values (in legend). The $q = 2$ surfaces are also indicated with horizontal lines.

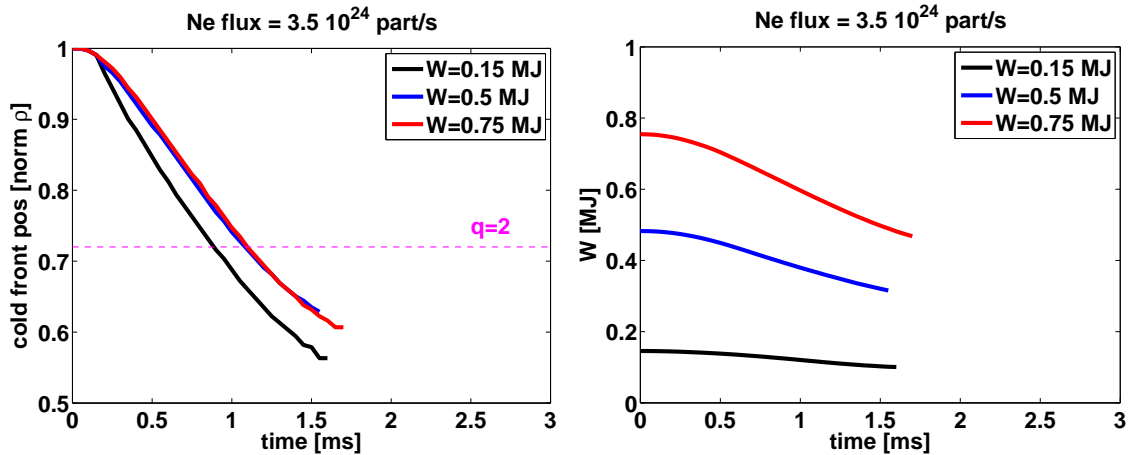


Figure 19. Time trace of (left plot) cold front position in normalized ρ for different plasma energies (in legend). (right plot) time trace of plasma thermal energy W [MJ].

4.3. Dependence of the pre-TQ time on the plasma stored thermal energy

It was observed that plasmas with very different stored energy exhibit very similar pre-TQ times, at the high levels of gas influx as used in the previous simulations. This observation requires understanding, since it is important for choosing the gas type and quantity for heat load mitigation, depending on the plasma scenario.

At first, the three discharges #30441 (L-mode, $W \sim 0.15$ MJ), #30440 (H-mode at moderate power, $W \sim 0.5$ MJ) and #30442 (H-mode at high power, $W \sim 0.75$ MJ) are simulated, employing the same gas-rate for each case. The max gas-rate is fixed at $\Phi = 3.5 \cdot 10^{24}$ [p/s]. In figure 19, the time traces of the cold front position (left plot) and

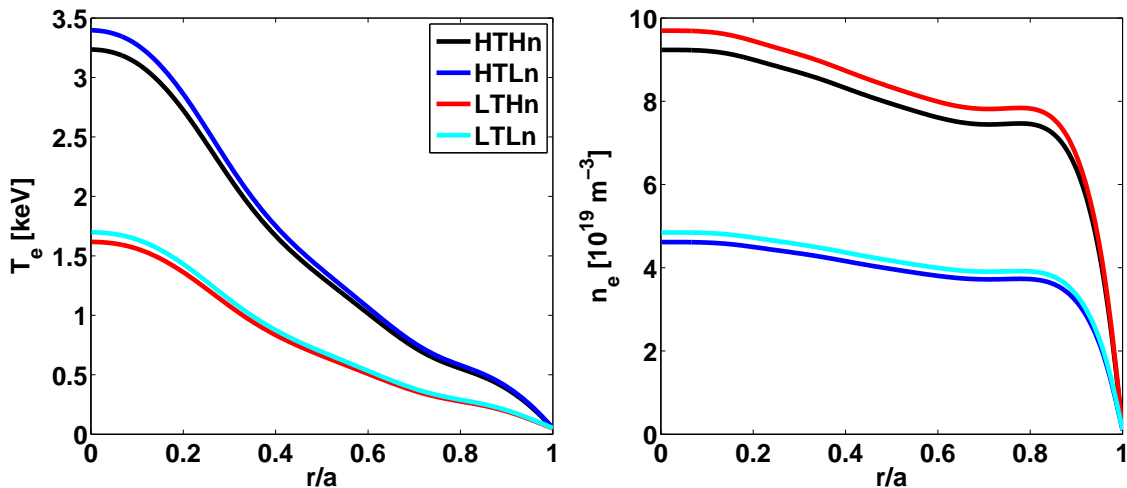


Figure 20. Left plot: T_e profiles. Right plot: n_e profiles.

of the plasma stored thermal energy W (right plot) are displayed, for the three cases (initial energy in legend). It is clear that the cold front propagation speed has very little variation among the three scenarios, despite the large difference (a factor of 5) between the L-mode and the high-power H-mode. Also, despite the gas-rate being the same, one observes that the instantaneous radiated power, during the cold front penetration, is somewhat proportional to the stored energy. To understand this, a separate scan has been performed in which, starting from a reference case (the $W = 0.5$ MJ case), density and temperature are separately rescaled to vary the plasma energy by one or the other parameter.

This separate study features a selective variation of the target plasma as shown figure 20. The four cases are labeled HTHn (high T_e , high n_e), HTLn (high T_e , low n_e), LTHn (low T_e , high n_e), LTLn (low T_e , low n_e). Cases HTLn, LTHn have half of the energy of HTHn, while LTLn has 0.25 times the energy of HTHn. For all these four cases, the injected Ne gas rate is the same.

In figure 21, left plot, the cold front penetration speed time traces are shown for the four cases. Practically no difference is found between the four cases, with a slightly higher max peak of the speed when decreasing T_e and/or n_e . It is also interesting to note that HTLn and LTHn, behave slightly different, with the case at lower temperature having the higher penetration speed. This suggests that the temperature has a larger effect in determining the penetration speed, although this is a very weak effect. In the right plot of figure 21, the time that the cold front takes to reach the $q = 2$ is shown against the initial plasma stored energy. The fit gives a very weak dependence, and two branches are found, connecting the highest with the intermediate energy. The upper branch is obtained by reducing the density, while the lower branch is obtained by reducing the temperature.

It is worth noticing that the energy dependence becomes stronger when reducing

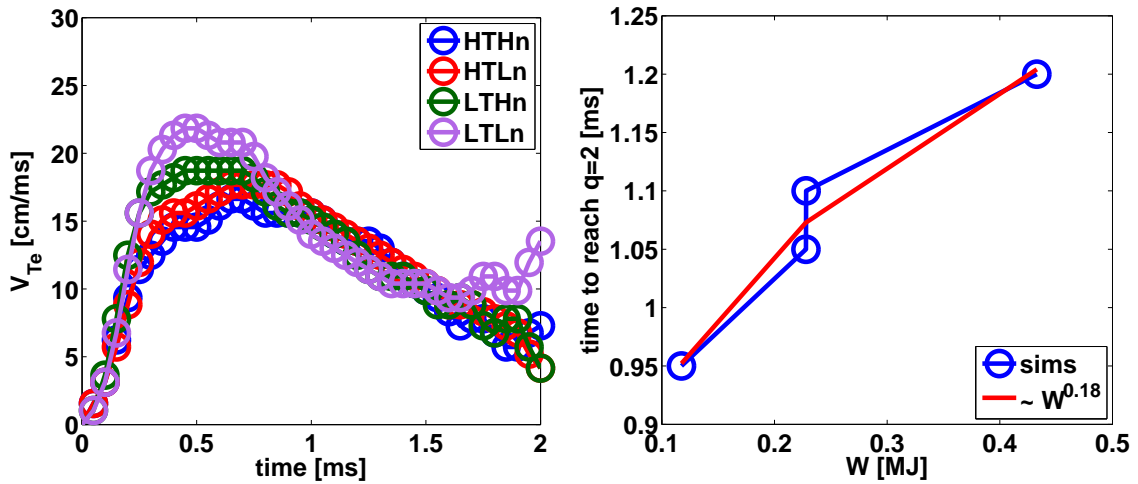


Figure 21. Left plot: time traces of the cold front penetration speed in [cm/ms]. Right plot: time for the cold front to reach $q = 2$ [ms] as a function of the plasma stored thermal energy.

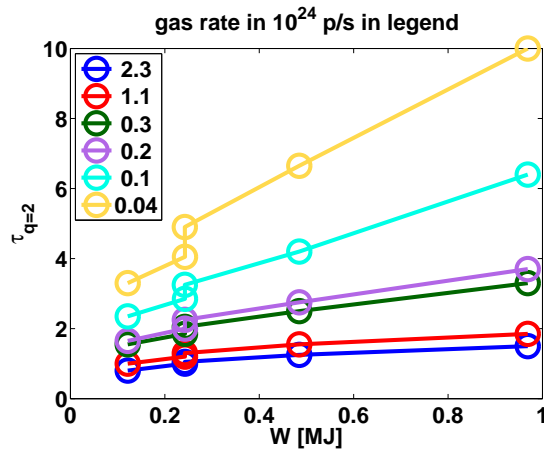


Figure 22. Time, in [ms], for the cold front to reach the $q = 2$ surface as a function of the plasma stored energy. In legend the values of the gas rate (units in the plot title) are shown.

the gas rate. The simulations show that by reducing the gas rate by a factor higher than 10, the pre-TQ time scales with the stored energy to power ~ 0.5 or slightly higher, in accordance with experimental observation. This is consistent with the change in exponent of the gas rate dependence. These two are in fact linked to the efficiency of gas "utilization" by the plasma, which is lower at higher gas rates. This behavior is shown in figure 22, where the time for the cold front to reach the $q = 2$ surface is plotted against the plasma stored energy, with the gas rate varying as indicated in legend. The plasma energy scan is done similarly as in figure 20, i.e. varying independently density and/or temperature. This plot shows that the energy dependence is stronger at lower

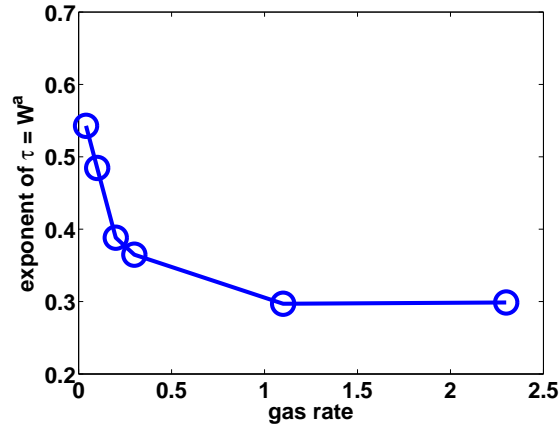


Figure 23. Exponent of the dependence $\tau_{q=2} \sim W^\gamma$ as a function of the gas rate.

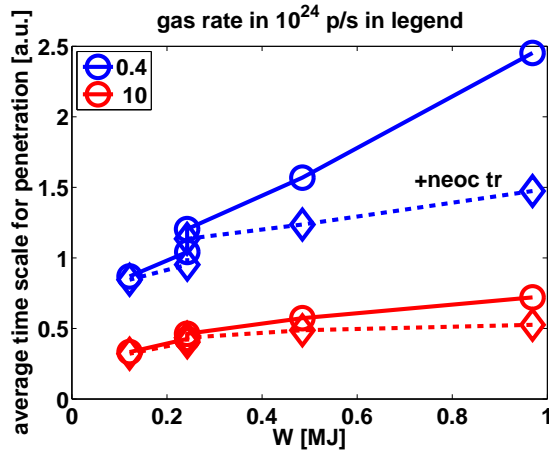


Figure 24. Average time scale for penetration of the cold front (estimated as inverse of average penetration speed over 3 ms) as a function of the plasma stored energy, for two gas rates (blue and red curves). Solid curves are obtained without neoclassical transport, while dashed curves are obtained by including neoclassical transport of Ne ions into account.

gas rate. The exponent γ of the scaling $\tau_{q=2} \sim W^\gamma$, is plotted in figure 23 as a function of the gas rate. The exponent is larger at lower gas rate, as expected.

The previous investigation on the energy/flux dependence has been carried out without impurity neoclassical transport. Upon including neoclassical transport, the energy dependence is weakened at all gas rates, thereby reducing the dependence at low gas rate, with respect to the previous case without neoclassical transport. This is shown in figure 24. There the "average time scale for penetration", estimated by computing the inverse of the average penetration speed for the first 3 ms of the cold front penetration (or up to the $q = 2$ in case that is reached before 3 ms) is plotted as a function of the plasma stored energy, for simulations without neoclassical transport (solid lines) and

with neoclassical transport (dashed lines). Two gas rates are shown, a low value (blue curves), and a high value (red curves). The explanation for the marked deviation of the cases with neoclassical transport from the cases without, at higher energies, can be attributed to the dominance of transport over radiation that starts to be visible at the higher energies, due to the elapsed time during penetration. In practice, since the cold front takes more time to penetrate at higher energies due to the low radiation (low gas rate), transport makes then most of the job. Of course one should question if neoclassical transport is here appropriately calculated as in reality the 3D structure of the cold front will deform the plasma equilibrium in a way as to eventually also alter neoclassical transport. However this cannot be accounted in our present model.

4.3.1. Explanation of the results of the energy scan at high gas rate. To understand the results displayed in figure 21, let us consider again equation (3), with dominant radiation as contributor to dT_e/dt , i.e. $V_{T_0} \sim L_Z n_Z a / T_e$.

Now by reducing n_e at fixed T_e , the neutrals are able to penetrate more due to the lower ionization rate, and since the Ne ions source is $n_e * n_{\text{neutrals}}$, the rate of generation of n_Z is more or less constant with n_e .

Then, by reducing T_e at fixed n_e , there are different effects that come into play. First L_Z could be slightly different due to transport. Then, the direct scaling $V_{T_0} \sim 1/T_e$ is not achieved due to the same reason of inefficient use of neutrals at higher speed, i.e. as speed increases due to lower temperature, at the same time the "effective" use of neutrals decreases, thus leading to a scaling $V_{T_0} \sim 1/T_e^\gamma$ with $\gamma < 1$.

The residual scaling of penetration speed on W as $\max(V_{T_0}) \sim W^{0.18}$ as shown in figure 21, right plot. As discussed previously, this dependence is relaxed towards larger exponents when decreasing the amount of injected neutrals.

4.4. Dependence of the pre-TQ time on the gas type and on the gas mixture

The simulations presented up to this point have been performed assuming Ne as the MGI species. However also deuterium and other noble gas species (and their mixture with deuterium) have been employed in experiments, since different species and mixtures are also being considered for the ITER DMS. If the impurity is a strong radiator at the relevant plasma temperatures, than the previous conclusions should apply irrespective of the exact impurity species. On the other hand, if low-Z impurities are used, then the questions of what determines the penetration speed is still open, as for pure deuterium, it does not radiate. Aside, CX losses could become important, something that is not taken into account here.

Two discharges, #30443 with a D MGI, and #30444 with He MGI, are simulated. For each case a scan in gas-rate is performed. Since the target plasma parameters are similar, as well as the post-MGI behavior, an additional simulation is performed with Ne, to check the sensitivity of the propagation speed on the impurity species. In figure 25(left) the average cold front penetration speed is plotted against the gas-rate.

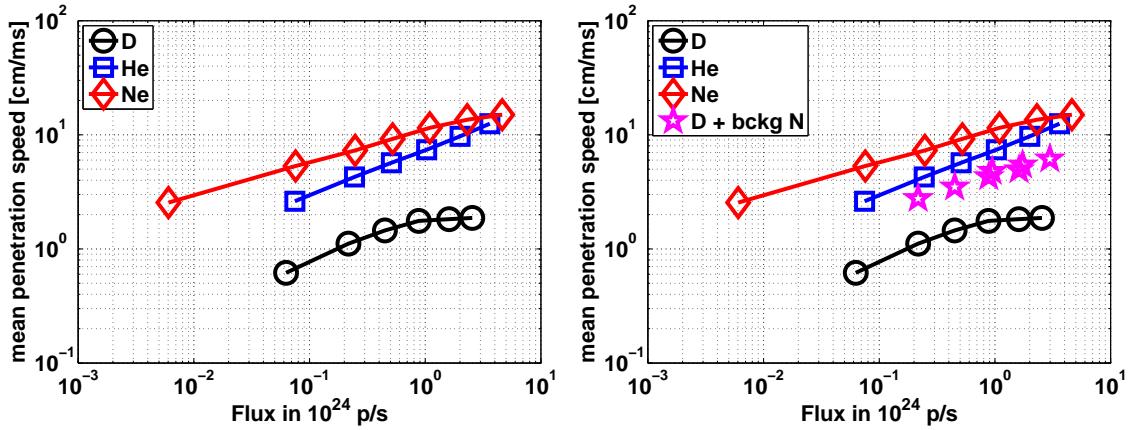


Figure 25. Left plot: comparison of cold front penetration speed (averaged over 1 ms time) versus the gas-rate. Different gas species are indicated in the legend. Right plot: same as left plot, but with addition of D MGI on top of background presence of N.

The average is taken over a 1 ms time period after the start of the MGI. It can be seen that D has a much lower penetration speed with respect to Ne, since in the case of D, the penetration is determined purely by dilution, with negligible radiation. In the case of He, at high gas-rates, radiation can become substantial (on top of stronger dilution) and provide a shorter pre-TQ time. In the experiment (pre-TQ time $\sim 1 - 3$ [ms]), He and D are both slower than Ne, however comparable (~ 3 [ms]). This means that in the case of D (and possibly of He), some other physics mechanisms contribute to the radiation losses and the T_e profile evolution.

One investigated possibility is the background impurities. A case with D MGI into a plasma with background N (in concentration to reach a $Z_{\text{eff}} \sim 1.6$) is simulated. The result is shown in figure 25(right). The new case is added. The penetration speed is larger than the case with D only, due to the N radiation when produced electrons are more and more due to the ionizing D. More experiments are needed to test the effect of the background impurities in the case of D, He MGI, also to disentangle this from transport effects that could cause a significant front acceleration.

4.5. Dependence of the pre-TQ time on the gas mixture

Of interest is also the case when the MGI consists of a mixture of high-Z/low-Z, for example Ne+D or Ar+He. In the present context, the choice has been to simulate a scan of Ne+D concentrations such that the total gas rate is constant, going from 0% to 90% D content. Discharge #30440 is used as the reference case to compare with the Ne only case. In figure 26, the time for the cold front to reach the $q = 2$ surface is shown against the Ne gas rate (i.e. the total gas rate rescaled by the Ne concentration in the mixture). On the other hand, for the Ne only case, the gas rate corresponds to the actual Ne rate. The result is that the inclusion of D does not bring any new physics

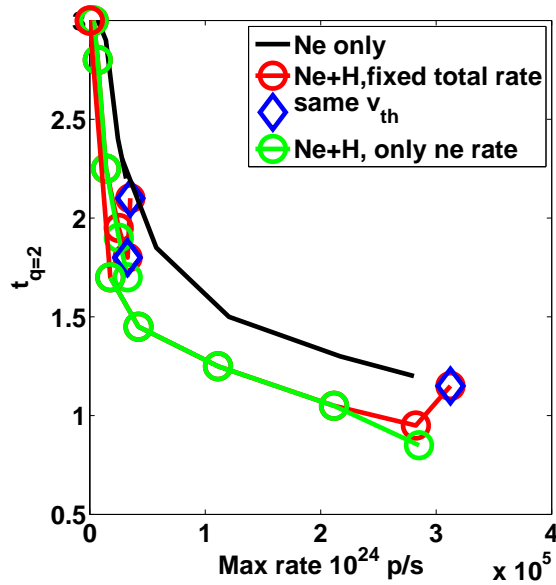


Figure 26. Time for the cold front to reach the $q = 2$ surface (in [ms]) as a function of the gas rate and gas mixture (described in the legend).

into play, except that lowering the Ne content increases the penetration time, following the same trend as found for the Ne only case. Note that the difference between Ne alone and Ne+D curves is given by neoclassical transport, that was switched on for the Ne+D case, and contributes a bit in decreasing the penetration time, since neoclassical transport increases strongly with collisionality.

A trial has also been made in changing the thermal velocity of the incoming neutrals, by matching D and Ne (while usually is the temperature of the neutrals that is equal). In this case nothing changes, which confirms that the neutral thermal speed being much faster than the cold front speed, has little impact on it.

5. Conclusions

Modeling of the pre-TQ time scale of AUG MGI scenarios has been carried out with the ASTRA-STRahl code package, featuring multi-species impurity calculations and the self-consistent evolution of temperatures, densities, and plasma current density. Mock-up of MHD-induced radial transport that could explain some features observed in the experiment, as e.g. spreading and acceleration of the radiation front has not yet been tested, but it is left for future work. The poloidal and toroidal symmetry is assumed in the 1D codes, while in reality the propagation of the gas is a 3D phenomenon, accompanied by 3D MHD activity and possible equilibrium distortion.

First simulations of a representative plasma discharge show rather good qualitative agreement between modeling and experiment. Also the time scale of the process seems to be already in the good ballpark of the measurements. A gas flux scan shows that

time scale/radiation/propagation speed are not linear in the flux, and also display some very interesting behavior that will be investigated further. The link between penetration speed and local radiated power is established, which allow to concentrate on the behavior of the radiated power. Of course comparison with other cases and sensitivity studies with respect to diffusivities will shed light on the exact role of equilibrium profiles and transient transport events and their influence on the pre-TQ duration.

Additional cases have been run, to explore the several dependencies (or absence of) as observed in the experiment. Energy, safety factor, gas species, and gas mixture dependencies have been studied, leading to positive identification of physics mechanisms that could be responsible for the observations. In some cases (safety factor, D MGI) it is still not clear which other mechanisms are responsible for the observed pre-TQ time, but everything seems to point into the direction of additional transport due to, for example, localized non-linear MHD, on top of growing macroscopic MHD driven by the 3D features of the MGI.

The energy dependence, which turns out to be very weak in the simulations, as observed in the experiment, is due to the interplay between neutral propagation through the cold region, transport, and radiative losses. This seems to hold very much independently on the scenario (aside from MHD) and should thus be reproducible on different machines and on ITER. This dependence is closely related to the weak gas-rate dependence, which seems to saturate at higher fluxes as reported in the intermediate report. This also is rather scenario-independent.

The role of different gas species seems to be clarified, although in the case of D and He, additional loss mechanisms could be important (CX, recombination).

In conclusion, it seems that the use of a 1D transport code, despite the obvious drawbacks in terms of geometry and MHD issues, is still leading to experimentally relevant results, most probably due to the very "simple" and localized nature of the radiative phenomenon (at least for the high-Z MGI). This can be summarized in figure 27, where the results of the Ne simulations (red curve) for the time scale of the cold front penetration is compared to a simple estimate: energy outside of the $q = 2$ surface divided by the maximum P_{rad} produced by the MGI. This correlation is also observed experimentally, as from figure (6), and it is thus an indicator that the 1D model is already good, if the radiative model is predicting the right amount of radiation for a given gas rate.

Acknowledgments This work has been funded under ITER contract IO/SGS/10086/AJB. The opinions expressed here do not necessarily reflect those of the ITER organization.

References

- [1] G. Pautasso et al., Nuclear Fusion **47** (2007) 900-913
- [2] C. Reux et al., Fusion Eng. and Design, **88** (2013) 1101-1104
- [3] E.M. Hollmann et al., Physics of Plasma **22**, 021802(2015)
- [4] M. Lehnen et al., Journal of Nuclear Material **463**, 39 (2015)

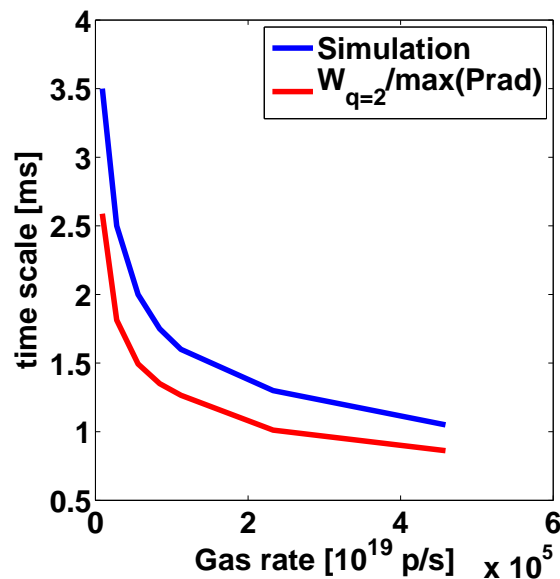


Figure 27. Comparison of cold front penetration time scale to reach the $q = 2$ surface for #30440 as a function of the gas rate, between actual simulation (blue curve), and simple estimate using the energy outside of the $q = 2$ surface and the maximum radiated power observed in the simulation.

- [5] S. Konovalov et al., Simulation of the Pre-Thermal Quench Stage of Disruptions at Massive Gas Injection and Projections for ITER, TH/P3-31, 25th IAEA Int. Conf. on Fusion Energy, St. Petersburg 2014
- [6] V. Izzo et al., *Phys. Plasmas*, **20** (2013) 056107
- [7] E. Nardon et al., contribution TH/P4-12 IAEA Conference 2014
- [8] G. Pautasso et al., *Nuclear Fusion*, **51** (2011) 103009
- [9] S. Pestchany et al., *Fusion Energy and Design* **96-97**, 685 (2015)
- [10] E. Hollmann et al., *Nucl. Fusion* **52**, 033001 (2012)
- [11] G. Pautasso et al., *Plasma Physics and Control Fusion* **1** (2009) 124056
- [12] M. Bernert et al., *Review of Scientific Instruments* **85** (2014) 033503
- [13] A. Mlynek et al., *Fusion Science and Technology* **61** (2012) 290
- [14] R. Fischer et al., *Fusion Science and Technology* **58** (2010) 675
- [15] G. Pautasso et al., *Nuclear Fusion* **55** (2015) 033015
- [16] G. Pautasso et al., *MGI in plasmas with locked modes*, Proc. 40th European Physical Society Conference on Plasma Physics (Espoo, Finland, 2013), paper O5.104
- [17] G. V. Pereverzev et al., Technical Report IPP 5/42, IPP, Garching, Germany (1991)
- [18] E. Fable et al., *Plasma Phys. Control. Fusion* **55**, 074007 (2013)
- [19] A. A. Ivanov et al., New Adaptive Grid Plasma Evolution Code SPIDER, 32nd EPS Conf. on Plasma Phys., ECA Vol.29C, P-5.063 (2005). Link: http://epsppd.epfl.ch/Tarragona/pdf/P5_063.pdf
- [20] R. Dux, <http://edoc.mpg.de/285559>
- [21] A. G. Peeters, *Phys. Plasmas* **7**, 268 (2000)
- [22] A. Fil et al., Modeling of disruption mitigation by massive gas injection in JET with JOREK and IMAGINE, 42nd EPS Conference on Plasma Physics, (2014), available at ocs.ciemat.es/EPS2015ABS/pdf/O4.135.pdf